ACS APPLIED ELECTRONIC MATERIALS

pubs.acs.org/acsaelm

Article

Optimized Doping of Diffusion Blocking Layers and Their Impact on the Performance of Perovskite Photovoltaics

Fedros Galatopoulos, Sapir Bitton, Maria Tziampou, Nir Tessler, and Stelios A. Choulis*

Cite This: ACS Appl. Electron. Mater. 2023, 5, 5580−5587

Read Online

ACCESS | Metrics & More | Article Recommendations | Supporting Information

ABSTRACT: The roll-to-roll printing production process for hybrid organic−inorganic perovskite solar cells (PSCs) demands thick and high-performance solution-based diffusion blocking layers. Inverted (p-i-n) PSCs usually incorporate solution-processed $PC_{70}BM$ as the electron-transporting layer (ETL), which offers good electron charge extraction and passivation of the perovskite active layer grain boundaries. Thick fullerene diffusion blocking layers could benefit the long-term lifetime performance of inverted PSCs. However, the low conductivity of $PC_{70}BM$ significantly limits the thickness of the $PC_{70}BM$ buffer layer for optimized PSC performance. In this work, we show that by applying just enough *N*-DMBI doping principle, we can maintain the power conversion efficiency (PCE) of inverted PSCs with a thick (200 nm) $PC_{70}BM$ diffusion blocking layer. To better understand the origin of an optimal doping level, we combined the experimental results with simulations adapted to the PSCs reported here. Importantly, just enough 0.3% wt *N*-DMBI-doped 200 nm $PC_{70}BM$ diffusion blocking layer-based inverted PCSs retain a high thermal stability at 60 °C of up to 1000 h without sacrificing their PCE photovoltaic parameters.

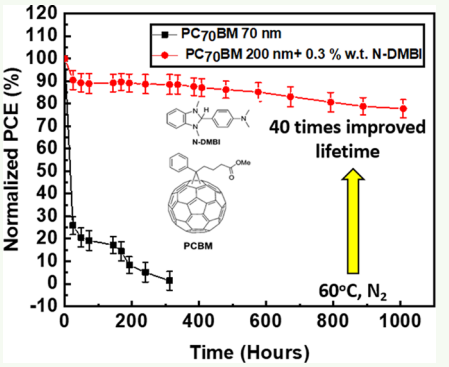

KEYWORDS: *perovskite solar cells, diffusion mechanisms, fullerenes, doping, conductivity, thermal stability, lifetime, electron-transporting layers*

1. INTRODUCTION

Over the past decade, research interest toward developing low-cost photovoltaic (PV) technologies has emerged. Solution-processed hybrid organic−inorganic perovskite solar cells (PSCs) have exhibited a substantial increase in their PCE from 3.8 to 25.7% certified PCE.[1,2] PSCs offer several advantages and attractive features, such as low exciton binding energy,[3,4] long carrier diffusion length,[5] high absorption coefficient,[6] tunable band gap,[7,8] and high carrier mobility.[9,10]

Although PSCs showed considerable advancement toward PCE, their long-term stability under high humidity, heat, and illumination conditions of such devices is still a major challenge that needs to be overcome.[11] The intrinsic stability, under humidity conditions, of the active layer is particularly poor due to the hygroscopic nature of perovskite cations, such as methylammonium (MA^+), which results in the decomposition of the perovskite crystal under moisture ingress.[12−15] Decomposition of the perovskite crystal has also been reported under exposure to atmospheric oxygen and ultraviolet illumination, which results in the formation of superoxide ions (O_2^-) and the deprotonation of MA^+ cations. Replacement of the organic cation by inorganic cations such as Cs was adopted as a strategy to improve the stability; however, fully inorganic PSCs are still lacking compared to their mixed halide counterparts in terms of their capability for large-solution-processed PSCs. Furthermore, other drawbacks of the fully inorganic PSC approach are their relatively large band gap and the lower absorption coefficient compared to mixed halide PSCs.[16] Furthermore, the organic cations incorporated in mixed halide PSCs help in the mitigation of nonradiative recombination as previously reported, providing at this stage at least higher PCE values.[17] High thermal conditions can affect the stability of PSCs as well, especially when combined with ambient environmental conditions. Heat can promote the diffusion of mobile anions such as I^- toward the electrodes of the device as well as promote the diffusion of metal atoms toward the active layer itself.[18−20] Several approaches were reported to mitigate these effects, such as the incorporation of metal oxides in the electrodes of the device, such as NiO_X[21] and γ-Fe_2O_3,[22] using a thin Cr layer to isolate the electrodes from the active layer[23] and utilization of amino acids either as cross-linkers[24] or for surface treatment and modification of the metal oxide under-layer electrodes.[25,26] Apart from improved stability, up-scalability of PSCs is also an important factor to consider in order to push PSCs toward

Received: July 5, 2023
Accepted: September 27, 2023
Published: October 12, 2023

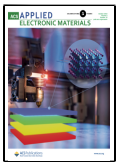

commercialization. Even though the aforementioned approaches have successfully improved the stability of PSCs, their incorporation into large-area PSC processing is not straightforward. Solution-processed fullerene buffer layers are an essential component of inverted perovskite PV device architecture, which can be easily upscaled for large-area processing. In our previous work, we showed a simple yet effective method to improve the thermal stability of PSCs utilizing thick fullerene diffusion blocking layers. However, we have also shown that by increasing the thickness of the fullerene layers, there is a dramatic drop of the FF and PCE due to the limited conductivity of the [6,6]-phenyl-butyric acid methyl ester (PCBM) even if the stability is improved.[18] Our previous experimental results on proposing thick fullerene diffusion blocking layers for long-lived PSCs also verified with the findings of Bitton et al[27] In their work, they have successfully simulated ionic diffusion in PSCs and have also shown that by increasing the thickness of PCBM from 50 to 200 nm, not only the ionic diffusion is prolonged but also the ionic accumulation at the contacts is significantly reduced, indicating that it will take at least 10 times longer to start observing some degradation by incorporating a 200 nm fullerene-based diffusion blocking layer within the inverted PSC device structure.[27]

Large-scale ETL fabrication techniques, such as Dr. Blade and roll−roll, are often utilized for the fabrication of large-scale PV devices.[28] Therefore, utilizing thick ETL layers that are compatible with such techniques is desirable for the increased scalability of PSCs. Currently, this is problematic when using $PC_{70}BM$ as the ETL for PSCs due to the limited conductivity of the material. One of the most well-known methods to improve the conductivity of $PC_{70}BM$ is via doping using n-type dopants, such as 4-(2, 3-dihydro-1, 3-dimethyl-1*H*-benzimidazol-2-yl)-*N* and *N*-dimethylbenzenamine (*N*-DMBI). This doping mechanism follows the general consensus that the dopant functions as a hydride atom donor to the host material ($PC_{70}BM$), followed by an electron transfer step between the molecules of the host material,[29] due to the natural affinity of $PC_{70}BM$ to undergo hydrogenation reactions with various hydrogen atom donors.[30] *N*-DMBI was reported to increase the conductivity of PCBM by 4−6 orders of magnitude (from $\sim 10^{-9}$ S/cm to 5×10^{-3} S/cm).[31−34] It has also been shown that PCBM exhibits a decrease of the Fermi level (E_F) from 5.04 to 4.78 eV toward the lowest unoccupied molecular orbital (LUMO), which further highlights the n-type doping of the material.[34] Therefore, n-type doping of PCBM with *N*-DMBI has been shown to be an effective and beneficial way to increase the conductivity and efficiency of devices, which has been demonstrated in various applications, such as organic photodiodes (OPDs)[31] and PSCs.[33,34] It is important to note that doping should usually follow the "just enough" concept, meaning that it should not exceed its optimal value. It has been suggested by Bitton et.al that when charge collection (CL) layers in PSCs are doped excessively, the device performance may degrade.[35] Here, we revisit that statement and show the negative effect of excess doping on the PSC lifetime. We use the same simulation as in ref 35 to shed light on the mechanism behind such optimal doping.

One of the biggest tasks in the design of high-performance inverted PCSs is the development of high-performance solution-processed diffusion blocking layers. In our previous work, we have shown that thick fullerene buffer layers improve the thermal stability of PSCs; however, the increase in fullerene buffet layer thickness was detrimental to the FF and PCE.[13] In this work, we have incorporated *N*-DMBI doping in conjunction with a thick (200 nm) $PC_{70}BM$ diffusion blocking layer to achieve thermally stable PSCs without sacrificing their photovoltaic (PV) parameters and PCE. In particular, using an optimum doping of 0.3% wt, we managed to improve the J_{SC} from 15.2 to 19 mA/cm^2, FF from 52.6 to 70.3%, and PCE from 7.84 to 13.1% when comparing thick (200 nm) undoped and doped $PC_{70}BM$-based devices while still retaining good thermal stability with T_{80}= 1000 h (time in which the PCE reached 80% of its initial value) under accelerated heat conditions (60 °C, N_2 atmosphere). The improvement of J_{SC} and FF is directly correlated to the increase in conductivity of $PC_{70}BM$, reduction of series resistance (R_S) from 13.1 to 1.5 Ω, and increase of shunt resistance (R_{SH}) from 41.7 to 50.2 kΩ. The optimum doping density is correlated to the iodide deficiency in the perovskite layer through the presented simulations.

2. RESULTS AND DISCUSSION

2.1. Solar Cell Device Structure and Electronic Film Characterization. The fabricated devices were based on the p-i-n inverted device structure of ITO/Cu:NiO_X/$CH_3NH_3PbI_3$/$PC_{70}BM$/BCP/Cu as shown in Figure 1a. The

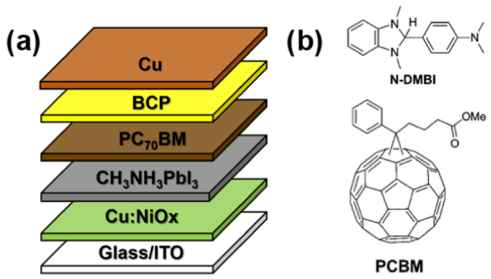

Figure 1. (a) Device architecture. (b) *N*-DMBI and fullerene schematic representation.

Cu:NiO_X was coated using Dr. Blade coating, followed by combustion synthesis, as described in detail in Section 4.[26] The perovskite active layer formulation was based on the solvent−antisolvent recipe used in our previous work and is described in detail in Section 4.[36,37] The $PC_{70}BM$ was spin-coated on the active layer, followed by thermal evaporation of the BCP and Cu films.

We fabricated ITO/$PC_{70}BM$ films to evaluate any potential morphological changes to the $PC_{70}BM$ due to doping. From the atomic force microscopy (AFM) data (Figure 2), we report

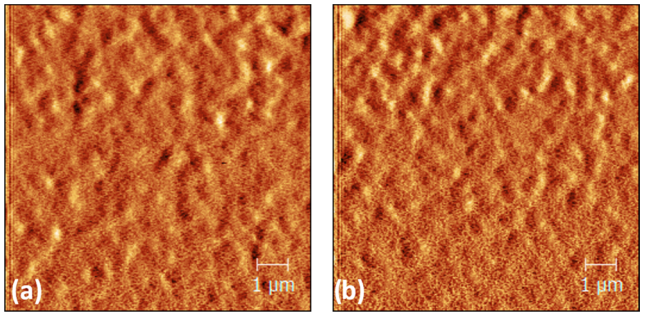

Figure 2. AFM measurements in phase contrast of (a) ITO/$PC_{70}BM$ pristine and (b) ITO/$PC_{70}BM$ (0.3% wt *N*-DMBI).

https://doi.org/10.1021/acsaelm.3c00900
ACS Appl. Electron. Mater. 2023, 5, 5580−5587

similar surface topography between ITO/$PC_{70}BM$ undoped and 0.3% doped films (which is later shown to be the optimum doping concentration). The compactness of the films is similar between the two films while also retaining similar roughness values (1.34 nm for ITO/$PC_{70}BM$ undoped and 1.25 nm for 0.3% doped films).

2.2. Characterization of Pristine and *N*-DMBI-Doped $PC_{70}BM$-Based Inverted Perovskite Solar Cells. To evaluate the effect of doping in devices with thick (200 nm) $PC_{70}BM$ ETLs, we have characterized both the light and dark J/V PV parameters when fresh as well as after aging at 60 °C on a hot plate inside a N_2-filled glovebox. Various *N*-DMBI doping concentrations (0.1, 0.3, 0.5, and 0.7% wt) were evaluated to identify the optimum value for devices based on thick $PC_{70}BM$ ETLs. When we increase the thickness of $PC_{70}BM$ from 70 to 200 nm, we see a decrease of V_{OC} from 1.02 to 0.98 V, J_{SC} from 18.04 to 15.2 mA/cm^2, FF from 78.5 to 52.5%, and PCE from 14.48 to 7.84% (Table 1), which is the same trend that we observed in our previous work.[18] The experimental values of J_{SC} are in good agreement with the theoretically calculated J_{SC} values from the EQE data, which is <5% in margin of error (Figure S1). This is also shown in the light and dark J/V plots (Figure 3a,b). An increase in R_S from 4.9 to 13.1 Ω and a decrease in R_{SH} from 53.1 to 41.7 kΩ, which results in the decrease of J_{SC}, V_{OC}, and FF, respectively, due to the limited conductivity of $PC_{70}BM$ are observed. This is further discussed in the impedance spectroscopy characterization. By introducing the optimum n-type doping concentration of *N*-DMBI (0.3% wt), we managed to decrease R_S from 13.1 to 1.5 Ω and increase R_{SH} from 41.7 to 50.2 kΩ, which in return improve the J_{SC} from 15.2 to 19 mA/cm^2, FF from 52.6 to 70.3%, and PCE from 7.84 to 13.1%. This improvement was reported in the literature to be due to the increase in conductivity and upshift of E_F, leading to the enhancement of electron-transporting properties of $PC_{70}BM$ and an increase of the photocurrent of the device.[33,34]

Table 1. Perovskite Solar Cell Photovoltaic Parameters

device structure	V_{oc} (V)	J_{sc} (mA/cm^2)	FF (%)	PCE (%)
ITO/Cu:NiO_X/$CH_3NH_3PbI_3$/PC_{70} BM (70 nm)/BCP/Cu	1.02	18.04	78.5	14.48
ITO/Cu:NiO_X/$CH_3NH_3PbI_3$/ $PC_{70}BM$ (200 nm)/BCP/Cu	0.98	15.2	52.6	7.84
ITO/Cu:NiO_X/$CH_3NH_3PbI_3$/ $PC_{70}BM$ (200 nm + 0.1% wt *N*-DMBI)/BCP/Cu	0.97	17.69	65.1	11.2
ITO/Cu:NiO_X/$CH_3NH_3PbI_3$/ $PC_{70}BM$ (200 nm + 0.3% wt *N*-DMBI)/BCP/Cu	0.98	19	70.3	13.1
ITO/Cu:NiO_X/$CH_3NH_3PbI_3$/ $PC_{70}BM$ (200 nm + 0.5% wt *N*-DMBI)/BCP/Cu	0.91	19.4	63	11.14
ITO/Cu:NiO_X/$CH_3NH_3PbI_3$/ $PC_{70}BM$ (200 nm + 0.7% wt *N*-DMBI)/BCP/Cu	0.90	17.83	58.5	9.45

When the doping concentration is increased from 0.3 to 0.5 and especially 0.7 wt %, a drop in V_{OC} and FF is observed as shown in Table 1. Therefore, the optimum doping concentration was identified to be 0.3% wt. The statistical distribution of the PCE for the devices characterized in Figure 3a is shown in Figure S2. The J/V characterization for 0.1, 0.3, 0.5, and 0.7% wt. *N*-DMBI-doped devices is shown in Figure S3.

Following the J/V characterization, we have performed impedance spectroscopy measurements to get more insight into the charge dynamics of the device. The impedance spectroscopy measurements presented in Figure 4 show two distinct frequency responses in the Nyquist plots, one at the high frequency (HF) range and one at the low frequency (LF) range. It has been previously reported for hybrid lead halide perovskite solar cells that the frequency response at HF is tied to the charge transport resistance (R_{TR}) of the solar cells, whereas the LF response is tied to the charge recombination resistance (R_{REC}) of the solar cell.[38,39]

An increase in R_{TR} is observed when we increase the thickness of $PC_{70}BM$ (Figure 4a), which is in accordance with the increase of R_S from the dark J/V plots due to the limited conductivity of the material. Upon introducing 0.3% wt *N*-DMBI, we see a decrease in R_{TR} similar to the decrease in R_S. Increasing the thickness of PC_{70} BM also reduces R_{REC} (Figure 4b), which is in accordance with the decrease of R_{SH}. R_{REC} is tied to the charge accumulation under illumination[37] at the electrodes of the device. Using thick $PC_{70}BM$, we introduce more charge recombination events in the ETL due to the increased trapping of the thick film and its limited conductivity. R_{REC} is substantially improved upon introducing 0.3% wt. *N*-DMBI, which can also be seen from the improvement of the FF, however, is still lower than the thin $PC_{70}BM$-based devices.

2.3. Accelerated Lifetime Performance and Simulation Studies of Pristine and *N*-DMBI-Doped $PC_{70}BM$ Diffusion Blocking Layer-Based Inverted Perovskite Solar Cells. Following the characterization of 0.3% wt *N*-DMBI-based devices, we have performed accelerated heat

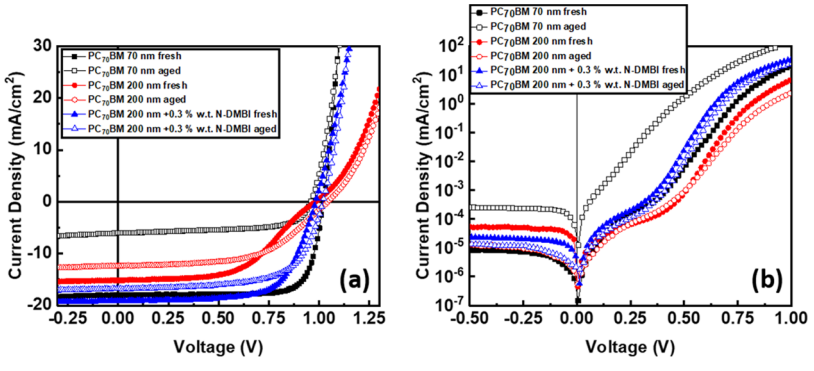

Figure 3. (a) Light J/V plots and (b) dark J/V plots of pristine and *N*-DMBI-doped $PC_{70}BM$ based devices.

https://doi.org/10.1021/acsaelm.3c00900
ACS Appl. Electron. Mater. 2023, 5, 5580−5587

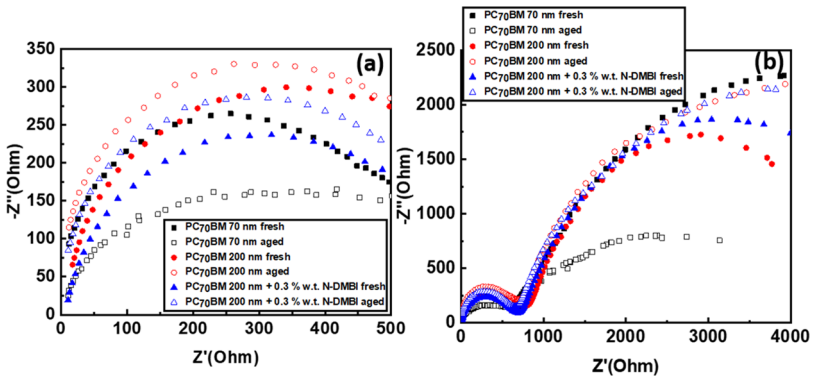

Figure 4. (a) Nyquist plot in high frequency and (b) Nyquist plot in low frequency.

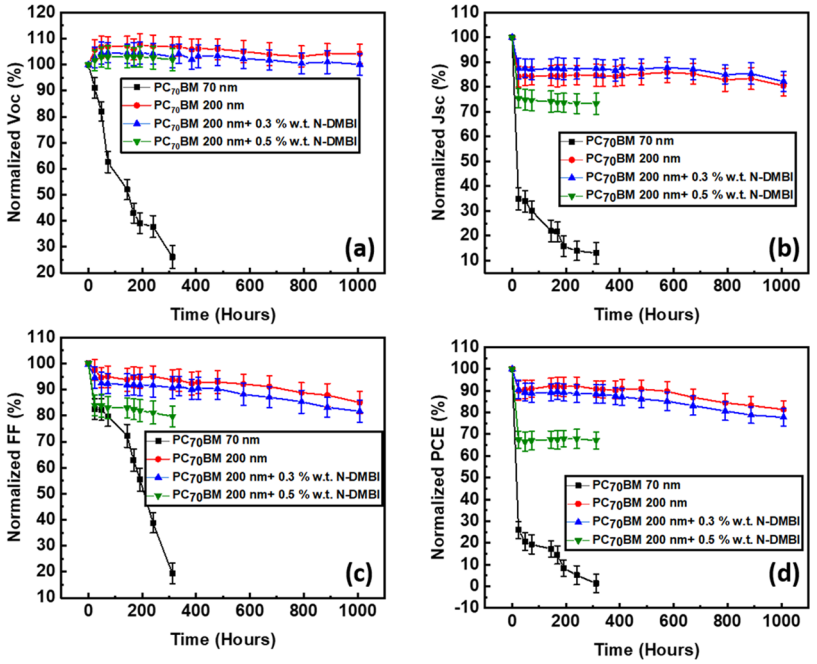

Figure 5. Normalized lifetime plots of (a) V_{OC}, (b) J_{SC}, (c) FF, and (d) PCE after aging in 60 °C, N_2.

lifetime tests (60 °C, N_2) to verify that the devices based on thick-doped $PC_{70}BM$ ETL not only had improved PV parameters but also retained a high lifetime. The goal of this work was not to achieve the highest possible PCE but to evaluate the application of thick fullerene diffusion blocking layers in conjunction with just enough doping to achieve high stability while still retaining a good compromise between the lifetime and PV performance. The J_{SC} trend is also visualized using photocurrent mapping (PCT) between fresh and aged devices. From the lifetime plots of Figure 5, we see that in our reference devices based on thin (70 nm) $PC_{70}BM$ ETL, there is a rapid drop in all PV parameters even at the first 24 h of aging. This drop in PCE has been previously identified to be a result of ion diffusion (especially I^-) toward the electrodes of the device.[18] By increasing the thickness of $PC_{70}BM$, the lifetime is improved, by functioning as a thick diffusion blocking layer, achieving T_{80} at 1000 h, however, as discussed previously in this report, this comes at an expense to the PCE of the device due to the limited conductivity of $PC_{70}BM$. Using 0.3% wt *N*-DMBI doped devices, we report improved lifetime while still retaining a good PCE. It is important to note that when the doping was increased from 0.3 to 0.5% wt *N*-DMBI, there was also a significant drop in efficiency at early times.

To visualize the trend of J_{SC} lifetime, we have performed (PCT) measurements for all of the devices evaluated. The results are presented in Figure 6. As shown, the trend of J_{SC} closely follows the PCT data. It is important to note that there is a slight increase in V_{OC} upon aging for the devices based on thick (200 nm) doped and undoped $PC_{70}BM$-based devices. It has been previously reported that heat treatment can promote $PC_{70}BM$ diffusion toward the grain boundaries of the perovskite active layer, assisting in their passivation.[40] Intentional doping of the perovskite active layer with $PC_{70}BM$ has been reported to improve the PV parameters of PSCs,[41] and we believe that in our case, a similar mechanism can happen due to a combination of large $PC_{70}BM$ thickness and its promoted diffusion due to the accelerated heat tests. This is further highlighted by the increase in R_{SH} from the dark J/V plots and R_{REC} from the Nyquist plots, which point toward reduced charge recombination, which can happen upon grain boundary passivation.

To better understand the origin of an optimal doping level, we performed simulations similar to those reported in ref 35,

https://doi.org/10.1021/acsaelm.3c00900
ACS Appl. Electron. Mater. 2023, 5, 5580−5587

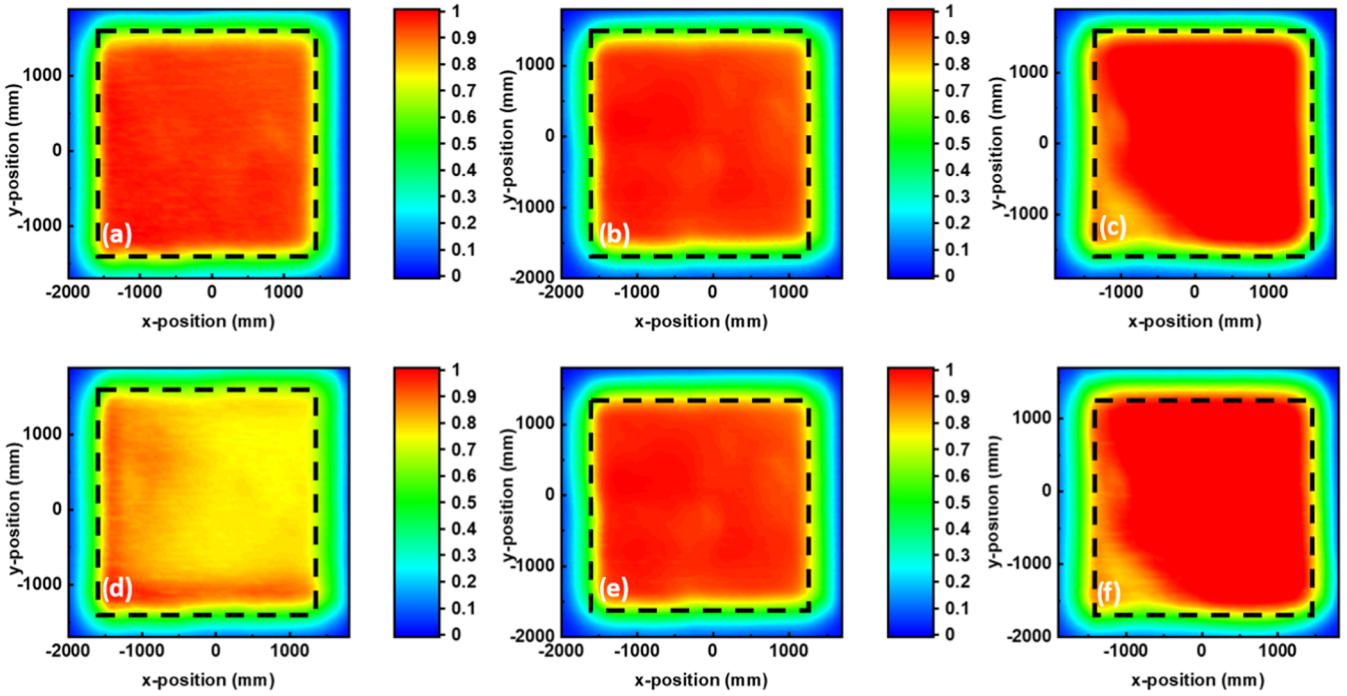

Figure 6. PCT data of $PC_{70}BM$-based devices: (a) 70 nm fresh, (b) 200 nm fresh, (c) 200 nm 0.3% wt *N*-DMBI fresh, (d) 70 nm aged, (e) 200 nm aged, and (f) 200 nm 0.3% *N*-DMBI aged.

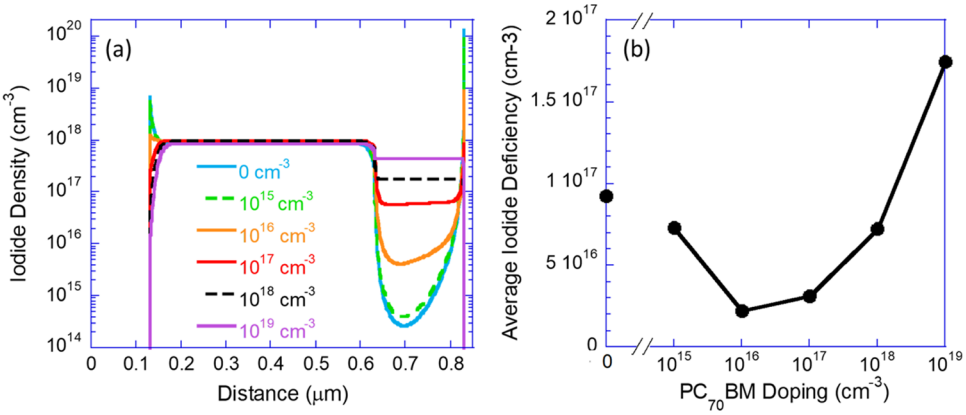

Figure 7. (a) Simulated iodide density distribution within the PSC for different doping levels of the electron transport layer (ETL). (b) Average iodide deficiency in the perovskite layer. The simulations were performed under 1 Sun and a bias close to the maximum power point.

with the device structure reported here. In short, we use a semiconductor device simulator by synopsis solving the drift-diffusion and Poisson equations for electrons, holes, and anions (iodide). The cations are taken to be static within the perovskite layer, and the initial ions' density within the perovskite layer was 10^{18} cm^{-3}. Figure 7a shows the iodide density distribution at a steady state under 1 Sun and a bias close to the maximum power point. The color coding marks the density of ionized N-type dopants at the electron transport layer (ETL). Due to noncomplete ionization, the actual dopant density could be significantly higher. The figure shows that the iodide penetrates the ETL and may accumulate at the contact interface. At low to no doping, the iodide is primarily close to the contact interface. As the doping density increases, the ETL is filled with iodide, while the density at the contact interface reduces. The trend shown in Figure 7a indicates that there should be an optimum doping density, and we show in Figure 7b the average deficiency of the iodide density in the perovskite layer as a function of the density of ionized dopants. This subfigure shows that there is an optimum at 10^{16} to 10^{17} cm^{-3} ionized dopants in the $PC_{70}BM$ layer.

The combined experimental and simulation results presented above show a clear correlation between $PC_{70}BM$ n-type doping and iodide distribution and experimentally verified the importance of just enough doping principle on the PSC lifetime performance.

3. CONCLUSIONS

In conclusion, we have shown that thick $PC_{70}BM$ ETLs can be successfully utilized as diffusion blocking layers for p-i-n inverted PSCs. By utilizing an optimal n-type doping concentration of 0.3% wt *N*-DMBI in conjunction with thick (200 nm) $PC_{70}BM$ ETLs, we have achieved highly stable (T_{80} = 1000 h under 60 °C, N_2) devices while still retaining relatively good PCE at 13.1%. By increasing the doping from 0.3 to 0.5 wt %, we observed a drop in the initial efficiency as

https://doi.org/10.1021/acsaelm.3c00900
ACS Appl. Electron. Mater. 2023, 5, 5580−5587

well as enhanced degradation. With the aid of the simulations, we correlate the experimental results with the penetration of iodide into the blocking layer and the corresponding iodide deficiency created in the perovskite photovoltaic active layer. Retaining a good PCE was mainly a result of improved J_{SC} and FF due to the improvement of the $PC_{70}BM$ conductivity, which resulted in a decrease of R_S from 13.1 to 1.5 Ω and an increase of R_{SH} from 41.7 to 50.2 kΩ. Utilizing a thick $PC_{70}BM$ diffusion blocking layer while still retaining a good compromise between the lifetime and PCE is important for the up-scalability of p-i-n- inverted PSCs and just enough doping is essential to retain this balance. The optimum doping density was correlated with the deficiency of iodide density in the perovskite layer through simulations. The proposed method of incorporating a 0.3% wt *N*-DMBI-doped thick fullerene diffusion blocking layer within the inverted PSC device architecture can be in practice easily applied to the roll-to roll printing manufacturing process providing a simple device engineering route for achieving high-performance PSCs.

4. EXPERIMENTAL METHODS

4.1. Materials. Toluene (99.7%), nickel(II) nitrate hexahydrate (>98.5%) ($Ni(NO_3)_2{\cdot}6H_2O$), copper(II) nitrate trihydrate (99−104%) ($Cu(NO_3)_2{\cdot}3H_2O$), 2-methoxyethanol anhydrous (99.8%), acetylacetone (≥99%), dimethyl sulfoxide (≥99.7%),γ-butyrolactone (≥99%), chlorobenzene anhydrous (99.8%), and 4-(2,3-dihydro-1, 3-dimethyl-1*H*-benzimidazol-2-yl)-*N*,*N*-dimethylbenzenamine (98%) were purchased from Sigma-Aldrich Chemicals. Methylammonium iodide (≥99%) was purchased from GreatCell Solar. Lead(II) iodide (99.999%) and bathocuproin (98%) were purchased from Alfa Aeser. Phenyl-C70-butyric acid methyl ester (99%) was purchased from Solenne BV. Cu pellets were purchased from Kurt J. Lesker. Ultrapure water was produced by a milli-Q Academic system, Millipore (Burlington, MA). All solutions were prepared with analytical grade chemicals and ultrapure milli-Q water with a conductivity of 18.2 μS/cm. ITO-patterned glass substrates (sheet resistance 4 Ω/sq) were purchased from Psiotec Ltd.

4.2. Cu:NiO_x Solution. For the combustion synthesis of Cu:NiO_x, 0.95 mmol of $Ni(NO_3)_2{\cdot}6H_2O$ and 0.05 mmol of $Cu(NO_3)_2{\cdot}3H_2O$ were dissolved in 2.5 mL of 2-methoxyethanol. The solutions were stirred at 50 °C for 1 h under ambient conditions, and then, 0.1 mmol of acetylacetone was added to the solution, and the whole solution was left for further stirring for 1 h at room temperature.

4.3. Perovskite Solution. The perovskite solution was prepared using a mixture of MAI/PbI_2 (1:1). The mixture was dissolved in a solvent of γ-butyrolactone/DMSO (7:3). The solution was stirred at 60 °C for 1 h in an inert atmosphere inside a N_2-filled glovebox. The perovskite solution was left to cool at room temperature inside the glovebox followed by filtering using a 0.22 μm PVDF filter.

4.4. $PC_{70}BM$ Solution. The $PC_{70}BM$ solution was prepared at concentrations of 20 mg/mL (for 70 nm films) and 50 mg/mL (for 200 nm films) in chlorobenzene. The solution was left overnight at 60 °C under ambient conditions.

4.5. *N*-DMBI Solution. *N*-DMBI solutions of various concentrations to achieve the required doping concentrations were prepared in CB and left overnight under stirring and at 60 °C under ambient conditions. The solutions were then mixed with the $PC_{70}BM$ solution the next day.

4.6. Device Fabrication. ITO-patterned glass substrates were cleaned using an ultrasonic bath for 10 min in acetone followed by 10 min in isopropanol. The Cu:NiO_x films (30 nm) were coated using a Doctor Blade with a blade speed of 5 mm/s and a plate temperature of 85 °C. The films were annealed at 300 °C on a hot plate for 1 h in ambient atmosphere. The perovskite films were coated inside a N_2 atmosphere glovebox using a three-step spin-coating process: first step, 500 rpm for 5 s; second step, 1000 rpm for 45 s; and third step, 5000 rpm for 45 s. During the third step, after the first 20 s of the duration of the step, 0.5 mL of toluene was dropped onto the spinning substrate as the antisolvent to achieve the rapid crystallization of the films. The resulting perovskite films (300 nm) were annealed at 100 °C for 10 min. The $PC_{70}BM$ film (70 and 200 nm depending on the concentration) was coated inside the glovebox by using spin coating at 1300 rpm for 30 s. The BCP (7 nm) and Cu layers (80 nm) were deposited using thermal evaporation.

4.7. Device Characterization. The thicknesses and surface profile of the device layers were measured with a Veeco Dektak 150 profilometer, Hong Kong, China. The current density−voltage (J/V) characteristics were characterized with a Botest LIV Functionality Test System (Kreuzwertheim, Germany). Both forward (short circuit−open circuit) and reverse (open circuit−short circuit) scans were measured with 10 mV voltage steps and 40 ms of delay time. For illumination, a calibrated Newport Solar simulator (Irvine, CA) equipped with a Xe lamp was used, providing an AM1.5G spectrum at 100 mW/cm^2, as measured by a certified Oriel 91,150 V calibration cell. A custom-made shadow mask was attached to each device prior to the measurements to accurately define the corresponding device area (9 mm^2). EQE measurements were performed by Newport System (Irvine, CA), Model 70356_70316NS. Impedance spectroscopy was performed using a Metrohm Autolab PGSTAT 302N equipped with the FRA32 M module (Herisau, Switzerland). To extract the Nyquist plots, the devices were illuminated using a white LED. A small AC perturbation voltage of 10 mV was applied, and the current output was measured at a frequency range of 1 MHz to 1 Hz. The steady-state DC bias was kept at 0 V. Atomic force microscopy (AFM) data was obtained using a Nanosurf easyScan 2 controller in tapping mode. Photocurrent (PCT) measurements were performed using a Botest Photoelectric Test System—PCT 1 equipped with a 405 nm laser at 25 mW power. The devices were taken outside the glovebox to measure their PV parameters and undergo device characterization at 24 h intervals as needed. The devices were placed back in the glovebox to continue the aging process every 24 h.

■ ASSOCIATED CONTENT

Supporting Information

The Supporting Information is available free of charge at https://pubs.acs.org/doi/10.1021/acsaelm.3c00900.

EQE data for thin (70 nm), thick (200 nm), and doped (0.3% wt *N*-DMBI) fresh and aged devices (Figure S1); statistical distribution of PCE for devices based on (a) $PC_{70}BM$ 70 nm, (b) $PC_{70}BM$ 200 nm, and (c) $PC_{70}BM$ 200 nm + 0.3% wt *N*-DMBI (Figure S2); and illuminated J/V characteristics of devices based on 0.1, 0.3, 0.5, and 0.7% wt *N*-DMBI doping (Figure S3) (PDF)

■ AUTHOR INFORMATION

Corresponding Author

Stelios A. Choulis − *Molecular Electronics and Photonics Research Unit, Department of Mechanical Engineering and Materials Science and Engineering, Cyprus University of Technology, Limassol 3603, Cyprus;* orcid.org/0000-0002-7899-6296; Email: Stelios.Choulis@cut.ac.cy

Authors

Fedros Galatopoulos − *Molecular Electronics and Photonics Research Unit, Department of Mechanical Engineering and Materials Science and Engineering, Cyprus University of Technology, Limassol 3603, Cyprus*

Sapir Bitton − *Sara and Moshe Zisapel Nano-Electronic Center, Department of Electrical Engineering, Technion-Israel, Institute of Technology, Haifa 32000, Israel*

Maria Tziampou − *Molecular Electronics and Photonics Research Unit, Department of Mechanical Engineering and*

https://doi.org/10.1021/acsaelm.3c00900
ACS Appl. Electron. Mater. 2023, 5, 5580−5587

Materials Science and Engineering, Cyprus University of Technology, Limassol 3603, Cyprus

Nir Tessler − *Sara and Moshe Zisapel Nano-Electronic Center, Department of Electrical Engineering, Technion-Israel, Institute of Technology, Haifa 32000, Israel;* orcid.org/0000-0002-5354-3231

Complete contact information is available at: https://pubs.acs.org/10.1021/acsaelm.3c00900

Notes

The authors declare no competing financial interest.

■ ACKNOWLEDGMENTS

This project has received funding from the European Research Council (ERC) under the European Union's Horizon 2020 research and innovation program (grant agreement No 647311).

■ REFERENCES

(1) Kojima, A.; Teshima, K.; Shirai, Y.; Miyasaka, T. Organometal Halide Perovskites as Visible-Light Sensitizers for Photovoltaic Cells. *J. Am. Chem. Soc.* **2009**, *131*, 6050−6051.

(2) NREL PV efficiency chart. 2021.

(3) Snaith, H. J. Perovskites: The Emergence of a New Era for Low-Cost, High-Efficiency Solar Cells. *J. Phys. Chem. Lett.* **2013**, *4*, 3623−3630.

(4) Stoumpos, C. C.; Malliakas, C. D.; Kanatzidis, M. G. Semiconducting Tin and Lead Iodide Perovskites with Organic Cations: Phase Transitions, High Mobilities, and Near-Infrared Photoluminescent Properties. *Inorg. Chem.* **2013**, *52*, 9019−9038.

(5) Noh, J. H.; Im, S. H.; Heo, J. H.; Mandal, T. N.; Seok, S. Il. Chemical Management for Colorful, Efficient, and Stable Inorganic−Organic Hybrid Nanostructured Solar Cells. *Nano Lett.* **2013**, *13*, 1764−1769.

(6) Liu, Y.; Bag, M.; Renna, L. A.; Page, Z. A.; Kim, P.; Emrick, T.; D Venkataraman, T. E.; Venkataraman, D.; Russell, T. P. Understanding Interface Engineering for High-Performance Fullerene/Perovskite Planar Heterojunction Solar Cells. *Adv. Energy Mater.* **2016**, *6*, No. 1501606.

(7) Savva, A.; Burgués-Ceballos, I.; Choulis, S. A. Improved Performance and Reliability of p-i-n Perovskite Solar Cells via Doped Metal Oxides. *Adv. Energy Mater.* **2016**, *6*, No. 1600285.

(8) Eperon, G. E.; Stranks, S. D.; Menelaou, C.; Johnston, M. B.; Herz, L. M.; Snaith, H. J. Formamidinium lead trihalide: a broadly tunable perovskite for efficient planar heterojunction solar cells. *Energy Environ. Sci.* **2014**, *7*, 982−988, DOI: 10.1039/c3ee43822h.

(9) Wehrenfennig, C.; Eperon, G. E.; Johnston, M. B.; Snaith, H. J.; Herz, L. M. High Charge Carrier Mobilities and Lifetimes in Organolead Trihalide Perovskites. *Adv. Mater.* **2014**, *26*, 1584−1589.

(10) Zhang, H.; Li, y.; Tan, S.; Chen, Z.; Song, K.; Huang, S.; Shi, J.; Luo, Y.; Li, D.; Meng, Q. High-efficiency (>20%) planar carbon-based perovskite solar cells through device configuration engineering. *J. Colloid Interface Sci.* **2022**, *608*, 3151−3158.

(11) Duan, L.; Uddin, A. Defects and stability of perovskite solar cells: a critical analysis. *Mater. Chem. Front.* **2022**, *6*, 400−417.

(12) Cao, J.; Yin, J.; Yuan, S.; Zhao, Y.; Li, J.; Zheng, N. Thiols as interfacial modifiers to enhance the performance and stability of perovskite solar cells. *Nanoscale* **2015**, *7*, 9443−9447.

(13) Fang, R.; Wu, S.; Chen, W.; Liu, Z.; Zhang, S.; Chen, R.; Yue, Y.; Deng, L.; Cheng, Y. B.; Han, L.; Chen, W. [6,6]-Phenyl-C 61 -Butyric Acid Methyl Ester/Cerium Oxide Bilayer Structure as Efficient and Stable Electron Transport Layer for Inverted Perovskite Solar Cells. *ACS Nano* **2018**, *12*, 2403−2414.

(14) Alsari, M.; Pearson, A. J.; Wang, J. T. S.; Wang, Z.; Montisci, A.; Greenham, N. C.; Snaith, H. J.; Lilliu, S.; Friend, R. H. Degradation Kinetics of Inverted Perovskite Solar Cells. *Sci. Rep.* **2018**, *8*, No. 5977.

(15) Chen, B.; Wang, S.; Song, Y.; Li, C.; Hao, F. A critical review on the moisture stability of halide perovskite films and solar cells. *Chem. Eng. J.* **2022**, *430*, No. 132701.

(16) Maafa, I. M. All-Inorganic Perovskite Solar Cells: Recent Advancements and Challenges. *Nanomaterials* **2022**, *12*, No. 1651, DOI: 10.3390/nano12101651.

(17) Zhang, X.; Turiansky, M. E.; Van de Walle, C. G. All-inorganic halide perovskites as candidates for efficient solar cells. *Cell Rep. Phys. Sci.* **2021**, *2*, No. 100604.

(18) Galatopoulos, F.; Papadas, I. T.; Armatas, G. S.; Choulis, S. A. Long Thermal Stability of Inverted Perovskite Photovoltaics Incorporating Fullerene-Based Diffusion Blocking Layer. *Adv. Mater. Interfaces* **2018**, *5*, No. 1800280.

(19) Aristidou, N.; Molina, I. S.; Chotchuangchutchaval, T.; Brown, M.; Martinez, L.; Rath, T.; Haque, S. A. The Role of Oxygen in the Degradation of Methylammonium Lead Trihalide Perovskite Photoactive Layers. *Angew. Chem., Int. Ed.* **2015**, *54*, 8208−8212.

(20) Thambidurai, M.; Omer, M. I.; Shini, F.; Dewi, H. A.; Jamaludin, N. F.; Koh, T. M.; Tang, H.; Mathews, N.; Dang, C. Enhanced Thermal Stability of Planar Perovskite Solar Cells Through Triphenylphosphine Interface Passivation. *ChemSusChem* **2022**, *15*, No. e202102189.

(21) Zhao, X.; Kim, H.-S.; Seo, J.-Y.; Park, N.-G. Effect of Selective Contacts on the Thermal Stability of Perovskite Solar Cells. *ACS Appl. Mater. Interfaces* **2017**, *9*, 7148−7153.

(22) Papadas, I. T.; Galatopoulos, F.; Armatas, G. S.; Tessler, N.; Choulis, S. A. Nanoparticulate Metal Oxide Top Electrode Interface Modification Improves the Thermal Stability of Inverted Perovskite Photovoltaics. *Nanomaterials* **2019**, *9*, No. 1616, DOI: 10.3390/nano9111616.

(23) Domanski, K.; Correa-Baena, J. P.; Mine, N.; Nazeeruddin, M. K.; Abate, A.; Saliba, M.; Tress, W.; Hagfeldt, A.; Grätzel, M. Not All That Glitters Is Gold: Metal-Migration-Induced Degradation in Perovskite Solar Cells. *ACS Nano* **2016**, *10*, 6306−6314.

(24) Yun, S.-C.; Ma, S.; Kwon, H.-C.; Kim, K.; Jang, G.; Yang, H.; Moon, J. Amino acid salt-driven planar hybrid perovskite solar cells with enhanced humidity stability. *Nano Energy* **2019**, *59*, 481−491.

(25) Ogomi, Y.; Tsukamoto, S.; Saitho, T.; Shen, Q.; Toyoda, T.; Yoshino, K.; Pandey, S.; Ma, T.; Hayase, S. All-Solid Perovskite Solar Cells with HOCO-R-NH 3 + I − Anchor-Group Inserted between Porous Titania and Perovskite. *J. Phys. Chem. C* **2014**, *118*, 16651−16659, DOI: 10.1021/jp412627n.

(26) Galatopoulos, F.; Papadas, I. T.; Ioakeimidis, A.; Eleftheriou, P.; Choulis, S. A. Surface Treatment of Cu:NiOx Hole-Transporting Layer Using β-Alanine for Hysteresis-Free and Thermally Stable Inverted Perovskite Solar Cells. *Nanomaterials* **2020**, *10*, No. 1961, DOI: 10.3390/nano10101961.

(27) Bitton, S.; Tessler, N. Electron/hole blocking layers as ionic blocking layers in perovskite solar cells. *J. Mater. Chem. C* **2021**, *9*, 1888−1894.

(28) Duan, C.; Peng, Z.; Colberts, F. J. M.; Pang, S.; Ye, L.; Awartani, O. M.; Hendriks, K. H.; Ade, H.; Wienk, M. M.; Janssen, R. A. J. Efficient Thick-Film Polymer Solar Cells with Enhanced Fill Factors via Increased Fullerene Loading. *ACS Appl. Mater. Interfaces* **2019**, *11*, 10794−10800.

(29) Naab, B. D.; Guo, S.; Olthof, S.; Evans, E. G. B.; Wei, P.; Millhauser, G. L.; Kahn, A.; Barlow, S.; Marder, S. R.; Bao, Z. Mechanistic Study on the Solution-Phase n-Doping of 1,3-Dimethyl-2-aryl-2,3-dihydro-1 H -benzoimidazole Derivatives. *J. Am. Chem. Soc.* **2013**, *135*, 15018−15025.

(30) Jin, C.; Hettich, R.; Compton, R.; Joyce, D.; Blencoe, J.; Burch, T. Direct Solid-Phase Hydrogenation of Fullerenes. *J. Phys. Chem. A* **1994**, *98*, 4215−4217.

(31) Shekhar, H.; Lami, V.; Solomeshch, O.; Fenigstein, A.; Tomer, L.; Becky, L.; Vaynzof, Y.; Tessler, N. Doping induced performance enhancement in inverted small molecule organic photodiodes operating below 1V reverse bias - Towards compatibility with CMOS for imaging applications. *Org. Electron.* **2019**, *67*, 1−9.

(32) Wang, Z.; McMeekin, D. P.; Sakai, N.; Van Reenen, S.; Wojciechowski, K.; Patel, J. B.; Johnston, M. B.; Snaith, H. J. Efficient and Air-Stable Mixed-Cation Lead Mixed-Halide Perovskite Solar Cells with n-Doped Organic Electron Extraction Layers. *Adv. Mater.* **2017**, *29*, No. 1604186.
(33) Bin, Z.; Li, J.; Wang, L.; Duan, L. Efficient n-type dopants with extremely low doping ratios for high performance inverted perovskite solar cells. *Energy Environ. Sci.* **2016**, *9*, 3424−3428.
(34) Kim, S. S.; Bae, S.; Jo, W. H. Performance enhancement of planar heterojunction perovskite solar cells by n-doping of the electron transporting layer. *Chem. Commun.* **2015**, *51*, 17413−17416.
(35) Bitton, S.; Tessler, N. Electronic-ionic coupling in perovskite based solar cells: Implications for device stability. *Appl. Phys. Lett.* **2020**, *117*, No. 133904.
(36) Ioakeimidis, A.; Papadas, I. T.; Tsikritzis, D.; Armatas, G. S.; Kennou, S.; Choulis, S. A. Enhanced photovoltaic performance of perovskite solar cells by Co-doped spinel nickel cobaltite hole transporting layer. *APL Mater.* **2019**, *7*, 021101.
(37) Galatopoulos, F.; Savva, A.; Papadas, I. T.; Choulis, S. A. The effect of hole transporting layer in charge accumulation properties of p-i-n perovskite solar cells. *APL Mater.* **2017**, *5*, No. 076102.
(38) Glatthaar, M.; Riede, M.; Keegan, N.; Hvid, S.; Zimmermann, B.; Niggemann, M.; Hinsch, A.; Gombert, A. Efficiency limiting factors of organic bulk heterojunction solar cells identified by electrical impedance spectroscopy. *Sol. Energy Mater. Sol. Cells* **2007**, *91*, 390−393.
(39) Guerrero, A.; Belmonte, G.-G.; Mora-Sero, I.; Bisquert, J.; Kang, Y. S.; Jacobsson, T. J.; Correa-Baena, J.-P.; Hagfeldt, A. Properties of Contact and Bulk Impedances in Hybrid Lead Halide Perovskite Solar Cells Including Inductive Loop Elements. *J. Phys. Chem. C* **2016**, *120*, 8023−8032.
(40) Said, A. A.; Xie, J.; Zhang, Q. Recent Progress in Organic Electron Transport Materials in Inverted Perovskite Solar Cells. *Small* **2019**, *15*, No. 1900854.
(41) Zhu, X.; Zhao, X.; Li, L.; Peng, Y.; Wei, W.; Zhang, X.; Su, M.; Wang, Y.; Chen, Z.; Sun, W. Perovskite Self-Passivation with PCBM for Small Open-Circuit Voltage Loss. *Energy Power Eng.* **2020**, *12*, 257−272.

https://doi.org/10.1021/acsaelm.3c00900
ACS Appl. Electron. Mater. 2023, 5, 5580−5587